Springer Acta Mechanica Sinica

• RESEARCH PAPER •

Acta Mech. Sin., Vol. 41, 124223 (2025)
https://doi.org/10.1007/s10409-024-24223-x

Modulation of transformation strain based on crystal orientation effects in NiTi shape memory alloy

Aimeng Zhang[1,2], Su Chen[1,3], Chenyang Du[1], Fa Wu[1,2*], Chun Li[1,2], and Shaobin Zhang[1,2*]

[1] *School of Mechanics, Civil Engineering and Architecture, Northwestern Polytechnical University, Xi'an 710072, China;*
[2] *Shenzhen Research Institute of Northwestern Polytechnical University, Shenzhen 518057, China;*
[3] *China Academy of Space Technology, Xi'an 710072, China*

Received September 27, 2024; accepted November 12, 2024; published online February 14, 2025

Equiatomic NiTi shape memory alloys (SMAs) can exhibit multiple martensitic transformations from a parent phase, significantly influencing the advanced macroscopic properties of SMAs, such as the large deformation/strain ability. A comprehensive atomic-scale understanding of the selection rule of the martensite phase/variant and its impact on the macroscopic mechanical behavior of SMA could be helpful for the development of high-performance SMAs. This work studies the transformation pathway, preferred martensite variant and corresponding macroscopic behavior of single crystal and bicrystal NiTi SMAs based on molecular dynamics and theoretical analysis. It is found that the transformation strain of single crystal NiTi is significantly influenced by the crystal orientation-dependent transformation pathway and martensite variant. The selection rule is that the transformation pathway and preferred martensite variant, leading to maximum transformation strains for each orientation, are energetically preferred. It can be predicted theoretically and agrees well with the molecular dynamic simulations. In addition, the stress-strain response of bicrystal NiTi can be modulated by changing its transformation pathway based on the orientation effect. This work provides atomic insights into the orientation-dependent deformation ability of NiTi and could be helpful for the development of high-performance SMAs through orientation modulation.

Transformation strain, Crystal orientation, Shape memory alloy, Martensite variant, Transformation pathway

Citation: A. Zhang, S. Chen, C. Du, F. Wu, C. Li, and S. Zhang, Modulation of transformation strain based on crystal orientation effects in NiTi shape memory alloy, Acta Mech. Sin. 41, 124223 (2025), https://doi.org/10.1007/s10409-024-24223-x

1. Introduction

NiTi shape memory alloys (SMAs) are widely applied in various industries (e.g., biomedical, aerospace, automotive) owing to their extraordinary deformation/strain recoverability based on the reversible phase transformations between austenite and martensite phases [1-3]. Under high temperature stress-free conditions, the austenite phase (B2) of NiTi SMA is characterized to be a high-symmetry cubic structure, which is normally regarded as the parent phase [4,5]. In a stress-induced phase transformation, multiple martensite phases with low-symmetry structures can be formed, i.e., $L1_0$ tetragonal [6], B19 orthorhombic [7], B19' monoclinic [8], R trigonal [9] and BCO base-centered orthorhombic phase [10], which gives rise to symmetry-related variants of martensite phases. Based on the rotational symmetry of the crystal lattice, the number of the possible martensite variants resulting from the phase transformation of a cubic to tetragonal, orthorhombic, and monoclinic lattices are 3, 6, 12, respectively [11,12]. The phase transformation from austenite to different martensite phases/variants plays a significant role in the transformation strain, which provides the main source of the recoverable deformation/strain of NiTi.

Previous studies have demonstrated that the type and morphology of martensite phases and variants can significantly influence the mechanical properties of NiTi SMAs, such as transformation strain, transformation stress, energy dissipation, etc. [13-16]. Particularly, the transfor-

---

*Corresponding authors. E-mail addresses: wufa_scbz@nwpu.edu.cn (Fa Wu); zhang.shaobin@nwpu.edu.cn (Shaobin Zhang)
Executive Editor: Wei Hong

mation strain directly influences the large and reversible deformation ability, which is one of the most important advantages of SMAs. However, due to the synergistic influence of different factors on the transformation behavior of polycrystalline NiTi, i.e., grain size [17], grain boundary [18,19], and texture [20,21], it is difficult to precisely predict the transformation pathways and the induced martensite variants by a theoretical model. Meanwhile, it is found that there is an apparent discrepancy between the existing theoretical predictions [22] and experimental observations [23] on the transformation pathways. The theoretical predictions of NiTi alloys indicate three transformation pathways: B2 ↔ B19', B2 ↔ R, and R ↔ B19' [22], but under fully annealed conditions, NiTi only undergoes the B2 ↔ B19', and the R phase is prohibited [23]. In this situation, the understanding of the mechanical behavior of NiTi with simple microstructures, such as single crystal and bicrystal, could provide a fundament for elucidating the transformation behaviors of polycrystalline SMAs with complicated microstructures. Up to now, recent studies have focused on the effect of crystal orientation on the mechanical properties of single crystal SMA, such as crack propagation [24,25], shock compression behavior [26-28], tensile-compressive asymmetry [29,30] and nanoindentation response [31], as well as the superelasticity in high-entropy alloy single crystals [32-34] and SMA with special structures [35-40]. Especially, the crystal orientation-dependent plastic deformation mechanisms and competition with phase transformation behavior have captured the interest of researchers [41-45]. It has been shown that the dominant plastic deformation of materials is affected by crystal orientation, including slip transfer across phase boundaries, phase transformation and the nucleation of shear bands. In addition, the misorientations of bicrystals [46,47] and grain orientation of nanocrystalline SMA [48] also significantly influence its superelasticity and plastic deformation. These experimental observations and theoretical analysis suggest that orientation-dependent mechanical properties are connected to the microstructure during phase transformation. A comprehensive atomic-scale understanding of the selection rules of martensite phases/variants could help describe and predict the orientation effects on the macroscopic mechanical behavior of SMAs.

In this work, the macroscopic mechanical properties of single crystal and bicrystal NiTi with different orientations are systematically studied from the view of the microstructure evolution, i.e., transformation pathways and preferred martensite variants, based on the molecular dynamics (MD) method. It's found that the orientation-dependent transformation strain is influenced by the transformation pathway and martensite variant. Additionally, the stress-strain response of bicrystal NiTi can be modulated by changing its transformation pathway based on the orientation effect. These findings provide valuable insights into the atomic-level understanding of the accurate control ability of SMAs, which can guide the development of high-performance SMAs.

2. Structure models and simulation methodology

The initial single crystal NiTi samples with different crystal orientations, and the ideal cubic austenite phase with B2 structure, are constructed with dimensions of 10 nm × 10 nm × 10 nm as shown in Fig. 1(a). The construction of our sample relies on crystal orientation (which is designated as integers), and β describes the orientation as the angle between the z direction of the simulation sample and the [001] direction of the austenite lattice. β ranges from 0° to

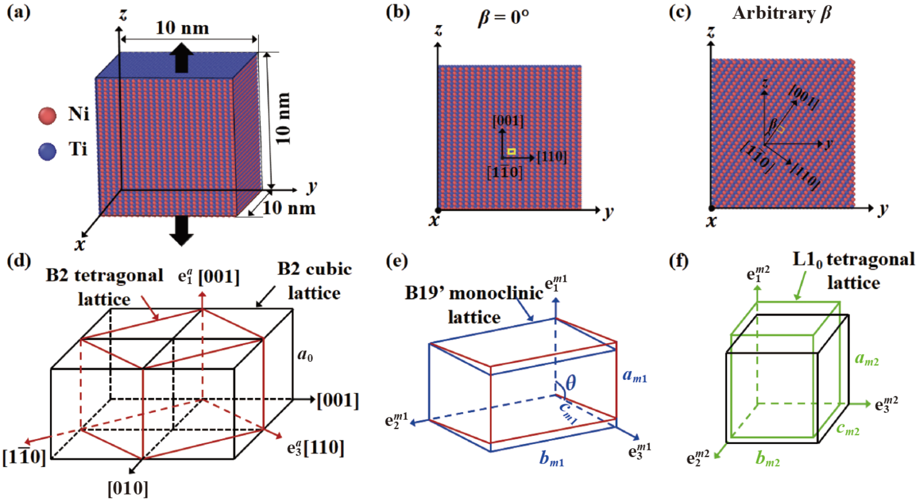

Figure 1 (a)-(c) Schematic of the samples with different orientations, which can be described by a rotation angle β ranging from 0° to 90° around the x-axis, i.e., β represents the angle between the z direction of the simulation sample and the [001] direction of the austenite lattice (depicted as the yellow squares in (b) and (c)). (d)-(f) The crystal structure of B2 austenite, B19' monoclinic and $L1_0$ tetragonal lattice, respectively.

90° and is not an integer when derived from the crystal orientation, as shown in Fig. 1(c). The strain-induced phase transformation of NiTi is performed based on the second nearest neighbor modified embedded-atom method (2NN-MEAM) potential [49] and the software LAMMPS [50]. To eliminate surface effects, periodic boundary conditions are applied along all three dimensions, following the approach used in previous literature [41,51]. Initially, all the samples are relaxed in an energy minimization process for a sufficient duration (100 ps) to obtain stable structures based on the conjugate gradient method [52] in the isobaric isothermal (NPT) ensemble. Meanwhile, the temperature is kept at 500 K, exceeding the austenite finish temperature (A_f) [51,53], which enables the maintenance of the B2 austenite phase in its zero-stress state. Then, a strain-controlled uniaxial tensile loading along the *z* direction of the relaxed samples is applied at a nominal strain rate of $5 \times 10^8\ \mathrm{s}^{-1}$ (the strain rate is in the conventional range of usual MD simulations, i.e., 10^7-$10^9\ \mathrm{s}^{-1}$ [54-57]). The maximum strain is set to ensure complete phase transformation of the specimens.

3. Results

3.1 Transformation behavior of single crystal NiTi with different orientations

Under strain-controlled tensile loading-unloading, the stress-strain responses of single crystal NiTi with different crystal orientations exhibit significant dependence on the crystal orientation, as shown in Fig. 2. With increasing β, the macroscopic responses during phase transformation change from a typical sigmoidal (i.e., "S"-shaped) stress-strain behavior (when $\beta = 0°$) to a two-stage transformation behavior (when $0° < \beta < 35.26°$). Then, when $\beta \geq 35.26°$, the stress decreases rapidly at the beginning of the phase transformation and then monotonically softens during the phase transformation as shown in Fig. 2(c). Meanwhile, it is noted that the transformation strain ε_tr varies non-monotonically against the crystal orientation as summarized in Fig. 3(a), i.e., with β increases from 0° to 35.26°, ε_tr decreases significantly from 14.2% to 7.1% then it fluctuates at around 7.1% until β increases to 90°. Here, ε_tr is determined by measuring the strain difference between the starting and the finishing of the phase transformation based on the volume fraction evolutions of different phases with the loading strain, as an example with $\beta = 19.47°$ shown in Fig. 3(b).

Microscopically, it is seen in Fig. 4 that both the transformation pathways and produced martensite variants depend on the crystal orientation. For the case of the sample with $\beta = 0°$ during loading in Fig. 4(a), the B2 austenite phase (see "a") transforms to pure $\mathrm{L1_0}$ phase (see "b"), followed by a reverse transformation to the B2 austenite phase during unloading (see "d") (i.e., pathway B2 → $\mathrm{L1_0}$ → B2). When β increases from 0° to 35.26°, as a typical example of $\beta = 10.02°$ shown in Fig. 4(b), the phase transformation occurs between a part of austenite and $\mathrm{L1_0}$ martensite (B2 → $\mathrm{L1_0}$ → B2), and between another part of austenite and B19' martensite (B2 → B19' → B2) during the loading-unloading process (see "b"). It means that both

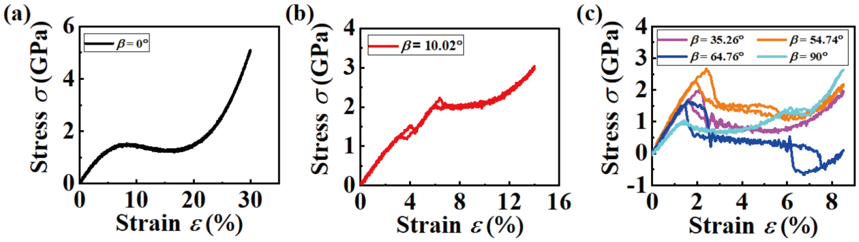

Figure 2 Stress-strain responses of NiTi with (a) $\beta = 0°$, (b) $\beta = 10.02°$, (c) $\beta \geq 35.26°$ during the tensile loading-unloading processes.

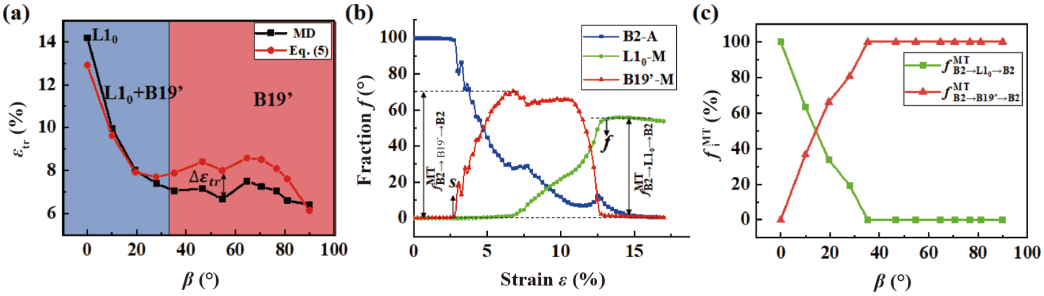

Figure 3 (a) Dependences of the transformation strain ε_tr on the crystal orientations. (b) The volume fraction evolution of each phase in an example with $\beta = 19.47°$ with the loading strain, "*s*" and "*f*" are the starting and finishing points of the phase transformation, respectively. The volume fraction of different transformation pathways is defined, e.g., the volume fraction of pathway B2 → B19' → B2 is the maximum fraction change of martensite B19'. (c) Dependences of the volume fractions of different transformation pathways f_i^MT on the crystal orientations.

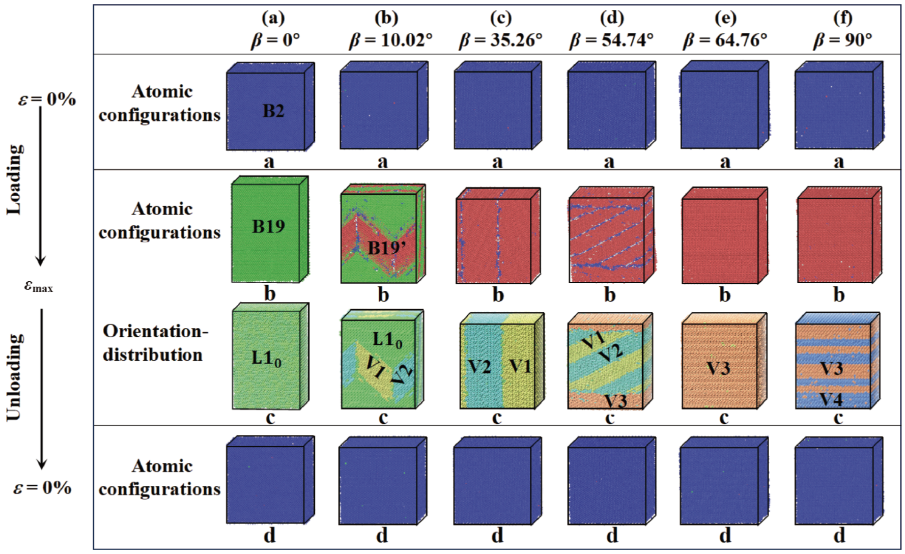

Figure 4 Atomic configurations of the samples with β from 0° to 90° at the initial state ($\varepsilon = 0\%$ at "a" line), after the maximum tensile loading ($\varepsilon = \varepsilon_{max}$ at "b" line) and after the unloading ($\varepsilon = 0\%$ at "d" line) process, where the blue atoms, green atoms, and red atoms correspond to the B2 austenite phase, $L1_0$ tetragonal martensite phase, and B19' monoclinic martensite phase, respectively. The variant distribution of the martensite phase after the maximum tensile loading ($\varepsilon = \varepsilon_{max}$ at "c" line) in order to identify the type of martensite variants.

pathways B2 → B19' → B2 and B2 → $L1_0$ → B2 occur in the samples with $0° < \beta < 35.26°$. Meanwhile, with β continuously increasing ($\beta \geq 35.26°$), the B2 austenite phase completely transforms to B19' martensite phase after loading and pathway B2 → B19' → B2 becomes the only transformation pathway as the examples shown in Fig. 4(d)-(f). The dependence of the transformation pathway on the crystal orientation is summarized in Fig. 3(c).

For more detailed martensite variants, it can be seen that only one type of $L1_0$ martensite variant is observed in all the samples after loading, but four types of B19' martensite variants can be formed depending on the crystal orientation as the variant distribution shown in line "c" in Fig. 4. The type of martensite variants and their respective volume fractions in samples with different orientations are shown in Fig. 5(a). In detail, for the samples with $\beta = 0°$, pathway B2 → $L1_0$ → B2 is the only transformation pathway and one type of $L1_0$ martensite variant (denoted as variants $L1_0$-1) exists as shown in Fig. 4(a). The lattice correspondence relationship between the austenite phase and variant $L1_0$-1 is: $[100]_{B2}//[100]_{L1_0\text{-}1}$, $[010]_{B2}//[010]_{L1_0\text{-}1}$, $[001]_{B2}//[001]_{L1_0\text{-}1}$, as shown in Fig. 1(f). For the samples with $0° < \beta < 35.26°$, both pathways B2 → B19' → B2 and B2 → $L1_0$ → B2 are the transformation pathways, in addition to variant $L1_0$-1, two types of B19' martensite variants (denoted as variants V1 and V2) occur, as an example with $\beta = 10.02°$ shown in Fig. 4(b). The monoclinic angles θ of variants V1 and V2 are the angles between [010] and [101] direction, and between [100] and $[01\bar{1}]$ direction, respectively, as shown in the insets in Fig. 5(a). When β increases from 35.26° to 90° ($35.26° \leq \beta \leq 90°$), pathway B2 → B19' → B2 is the only

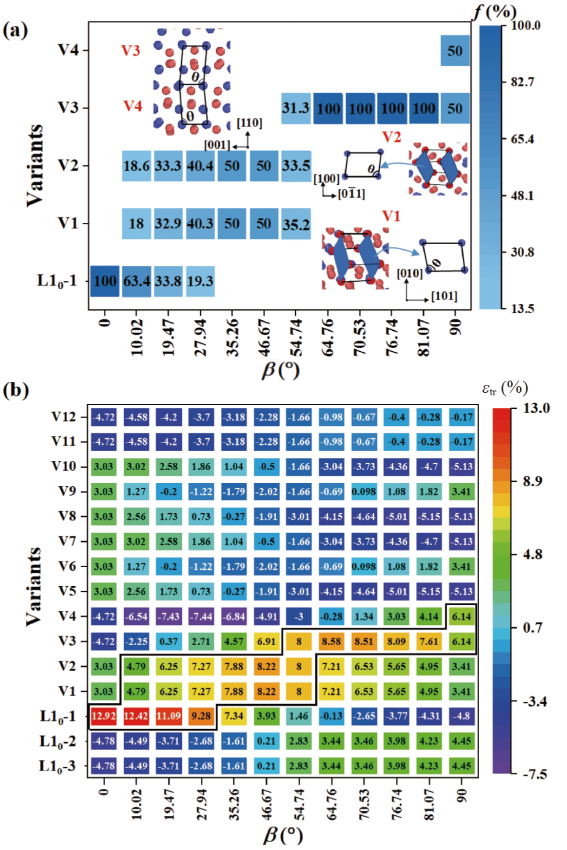

(a)

Variants	0	10.02	19.47	27.94	35.26	46.67	54.74	64.76	70.53	76.74	81.07	90
V4												50
V3							31.3	100	100	100	100	50
V2		18.6	33.3	40.4	50	50	33.5					
V1		18	32.9	40.3	50	50	35.2					
$L1_0$-1	100	63.4	33.8	19.3								

(b)

Variants	0	10.02	19.47	27.94	35.26	46.67	54.74	64.76	70.53	76.74	81.07	90
V12	-4.72	-4.58	-4.2	-3.7	-3.18	-2.28	-1.66	-0.98	-0.67	-0.4	-0.28	-0.17
V11	-4.72	-4.58	-4.2	-3.7	-3.18	-2.28	-1.66	-0.98	-0.67	-0.4	-0.28	-0.17
V10	3.03	3.02	2.58	1.86	1.04	-0.5	-1.66	-3.04	-3.73	-4.36	-4.7	-5.13
V9	3.03	1.27	-0.2	-1.22	-1.79	-2.02	-1.66	-0.69	0.098	1.08	1.82	3.41
V8	3.03	2.56	1.73	0.73	-0.27	-1.91	-3.01	-4.15	-4.64	-5.01	-5.15	-5.13
V7	3.03	3.02	2.58	1.86	1.04	-0.5	-1.66	-3.04	-3.73	-4.36	-4.7	-5.13
V6	3.03	1.27	-0.2	-1.22	-1.79	-2.02	-1.66	-0.69	0.098	1.08	1.82	3.41
V5	3.03	2.56	1.73	0.73	-0.27	-1.91	-3.01	-4.15	-4.64	-5.01	-5.15	-5.13
V4	-4.72	-6.54	-7.43	-7.44	-6.84	-4.91	-3	-0.28	1.34	3.03	4.14	6.14
V3	-4.72	-2.25	0.37	2.71	4.57	6.91	8	8.58	8.51	8.09	7.61	6.14
V2	3.03	4.79	6.25	7.27	7.88	8.22	8	7.21	6.53	5.65	4.95	3.41
V1	3.03	4.79	6.25	7.27	7.88	8.22	8	7.21	6.53	5.65	4.95	3.41
$L1_0$-1	12.92	12.42	11.09	9.28	7.34	3.93	1.46	-0.13	-2.65	-3.77	-4.31	-4.8
$L1_0$-2	-4.78	-4.49	-3.71	-2.68	-1.61	0.21	2.83	3.44	3.46	3.98	4.23	4.45
$L1_0$-3	-4.78	-4.49	-3.71	-2.68	-1.61	0.21	2.83	3.44	3.46	3.98	4.23	4.45

Figure 5 (a) The produced martensite variants and their corresponding volume fractions in samples with different orientations in MD results, and blank areas denote that the variant doesn't occur in the sample. The insets show the crystal structures of variants V1 to V4. (b) The transformation strain ε_{tr} from austenite to each of 12 types of B19' martensite phases and 3 types of $L1_0$ martensite phases along different orientations. The preferred martensite variants and corresponding transformation strains are marked by black box.

transformation pathway and four types of B19’ martensite variants can be observed. Variants V1 and V2 occur in the samples with 35.26° ≤ β < 54.74° as an example with β = 35.26° shown in Fig. 4(c). For the sample with β = 54.74°, in addition to variants V1 and V2, another type of martensite variant (denoted as V3) appears as shown in Fig. 4(d). The monoclinic angle θ of variant V3 is the angle between [001] and [110] direction, as shown in the insets in Fig. 5(a). Then, a single-variant V3 occupies the sample with 54.74° < β < 90°, and in addition to V3, a new martensite variant V4 appears in the sample with β = 90°, which is symmetrical in the monoclinic direction with variant V3 (see the lattice structure of V4 in the insets in Fig. 5(a)). The lattice correspondence relationships between the B2 austenite and variants V1-V4 are provided, respectively in Figs. S1-S4 in Supporting Information. The dependence of transformation strain on crystal orientation is primarily attributed to the orientation-dependent martensite variants, as will be discussed in detail in Sect. 4.1.

3.2 Transformation behavior of bicrystal NiTi

The <1$\bar{1}$0> symmetric tilt grain-boundary (STGB) samples composed of two single crystal grains with symmetric orientations (β_1 = β_2) and the <1$\bar{1}$0>asymmetric tilt grain boundary (ATGB) samples composed of two single crystal grains with asymmetric orientations ($\beta_1 \neq \beta_2$) are constructed with dimensions of 10 nm × 10 nm × 15 nm as shown in Fig. 6. Compared with the STGB sample, the type of ATGB sample is more complex due to the different crystal orientations of Grains 1 and 2. According to the different types of transformation pathways in single crystal NiTi, the orientations of single crystals can be divided into three categories, i.e., I: β = 0° (pathway B2 → L1_0 → B2), II: 0° < β < 35.26° (pathways B2 → L1_0 → B2 and B2 → B19’ → B2), and III: β ≥ 35.26° (pathway B2 → B19’ → B2). Here, the crystal orientations of the two grains in the ATGB sample are set as all possible combinations of three categories of the transformation pathway of single crystals, which are summarized in Table 1.

Under uniaxial tensile loading along z-axis, it is seen that the stress-stain responses of both STGB and ATGB samples depends on the crystal orientations also, as shown in Figs. 7 and 8. For the ATGB sample, the dependence of stress-strain response on orientation is more significant, e.g., the samples C and D exhibit nearly linear stress-strain curves, while the traditional strain softening occurs in other samples, particularly the sample E, as shown in Fig. 8. In the case of the STGB samples, all the stress-strain responses exhibit strain softening, while the transformation strain $\varepsilon_{\mathrm{tr}}$ depends on the crystal orientation, as shown in Fig. 7. Similar to the single crystal, $\varepsilon_{\mathrm{tr}}$ is determined based on the volume fraction evolutions of different phases with the loading strain (see Fig. S5) and summarized in Fig. 9. It is shown that $\varepsilon_{\mathrm{tr}}$ varies

Table 1 All possible ATGB samples (named A to F) and the corresponding crystal orientations of the two grains are set based on three categories of the transformation pathway of single crystals[a)]

Orientation categories	I	II			III		
		Sample		β (°)	Sample		β (°)
I	×	A	Grain 1	10.02	C	Grain 1	90
			Grain 2	0		Grain 2	0
II	×	B	Grain 1	10.02	D	Grain 1	46.67
			Grain 2	19.47		Grain 2	10.02
III	×	×			E	Grain 1	81.07
						Grain 2	64.76
					F	Grain 1	76.74
						Grain 2	46.67

a) I, II and III represent pathway B2 → L1_0 → B2, the coexistence of pathways B2 → L1_0 → B2 and B2 → B19’ → B2, and pathway B2 → B19’ → B2, respectively. The note × means the impossibility of forming or repeatedly forming ATGB samples.

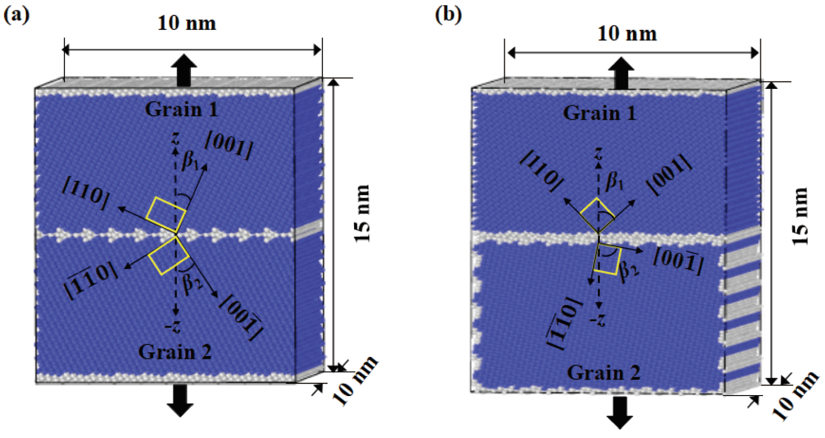

STGB sample ($\beta_1 = \beta_2$)

ATGB sample ($\beta_1 \neq \beta_2$)

Figure 6 Schematic of (a) the STGB ($\beta_1 = \beta_2$) and (b) ATGB samples ($\beta_1 \neq \beta_2$) with different crystal orientations, respectively. The blue and gray atoms correspond to the austenite (B2) structure and disorder structure, respectively.

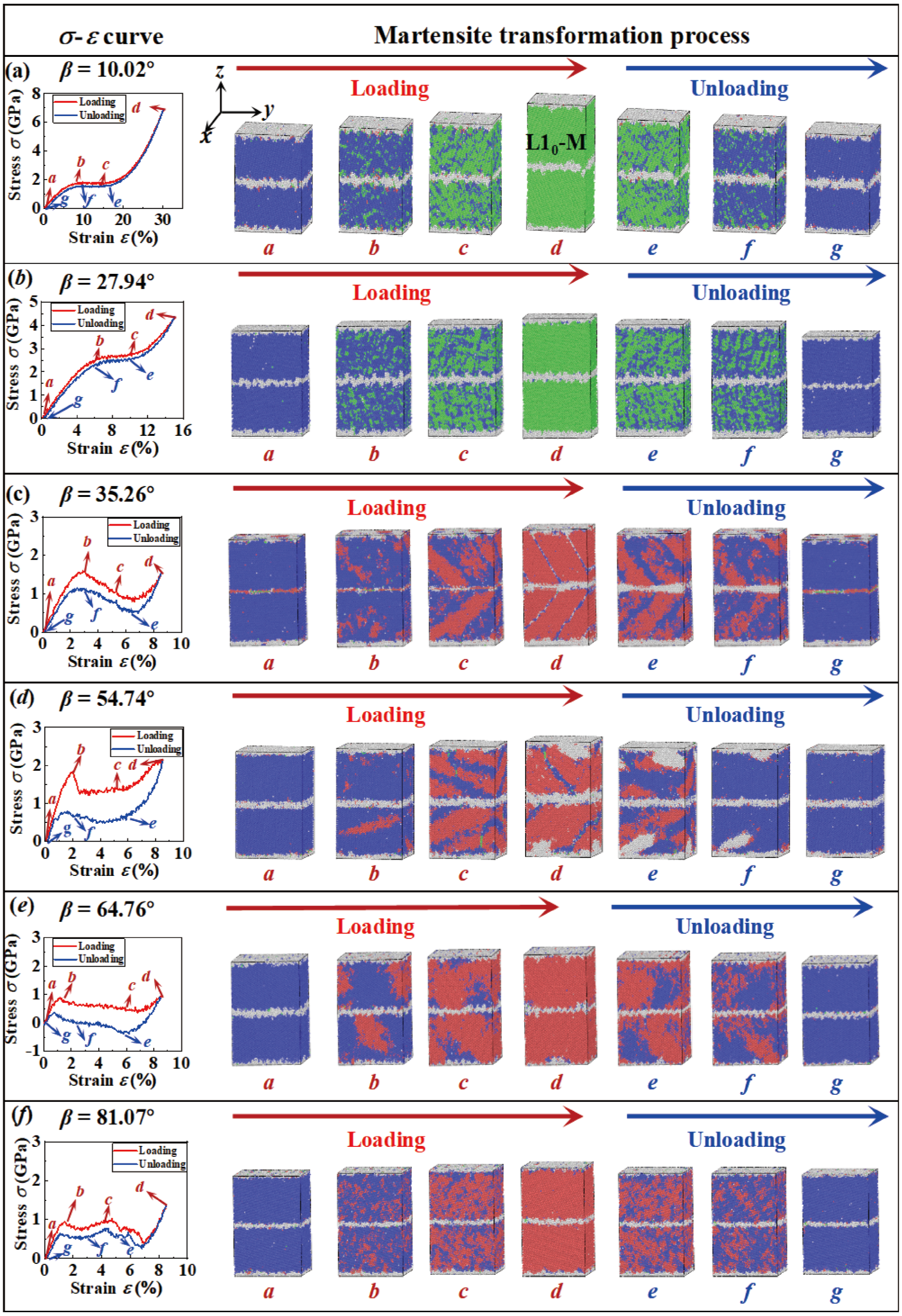

Figure 7 Stress-strain responses and atomic configurations of STGB samples with different orientations under the tensile loading-unloading process along the *z*-axis. The blue, red, green and gray atoms correspond to the austenite (B2), martensite (B19'), martensite ($L1_0$), and disorder structures, respectively.

non-monotonically against the crystal orientation, i.e., with β increases from 0° to 35.26°, $\varepsilon_{\rm tr}$ decreases significantly from 11.75% to 6.80%, then fluctuates around 6.80% with β increases to 90°, which is similar to the trend of $\varepsilon_{\rm tr}$ in single crystal NiTi, as shown in Fig. 9. Moreover, the magnitude of the transformation strain observed in the STGB sample closely approximates that of the single crystal with the corresponding orientation. These mechanical characteristics may be related to the synergistic effect of different transformation pathways resulting from the different orientations of both grains in the bicrystal sample.

Microscopically, the transformation pathway of the STGB and ATGB samples are shown in Figs. 7 and 8, which can be inferred based on the transformation pathway of the single crystal with the corresponding orientation. For the orientation categories I (β = 0°) and III ($\beta \geq 35.26°$), where the single crystal NiTi takes only one transformation pathway (pathway B2 → $L1_0$ → B2 for the sample with β = 0° and

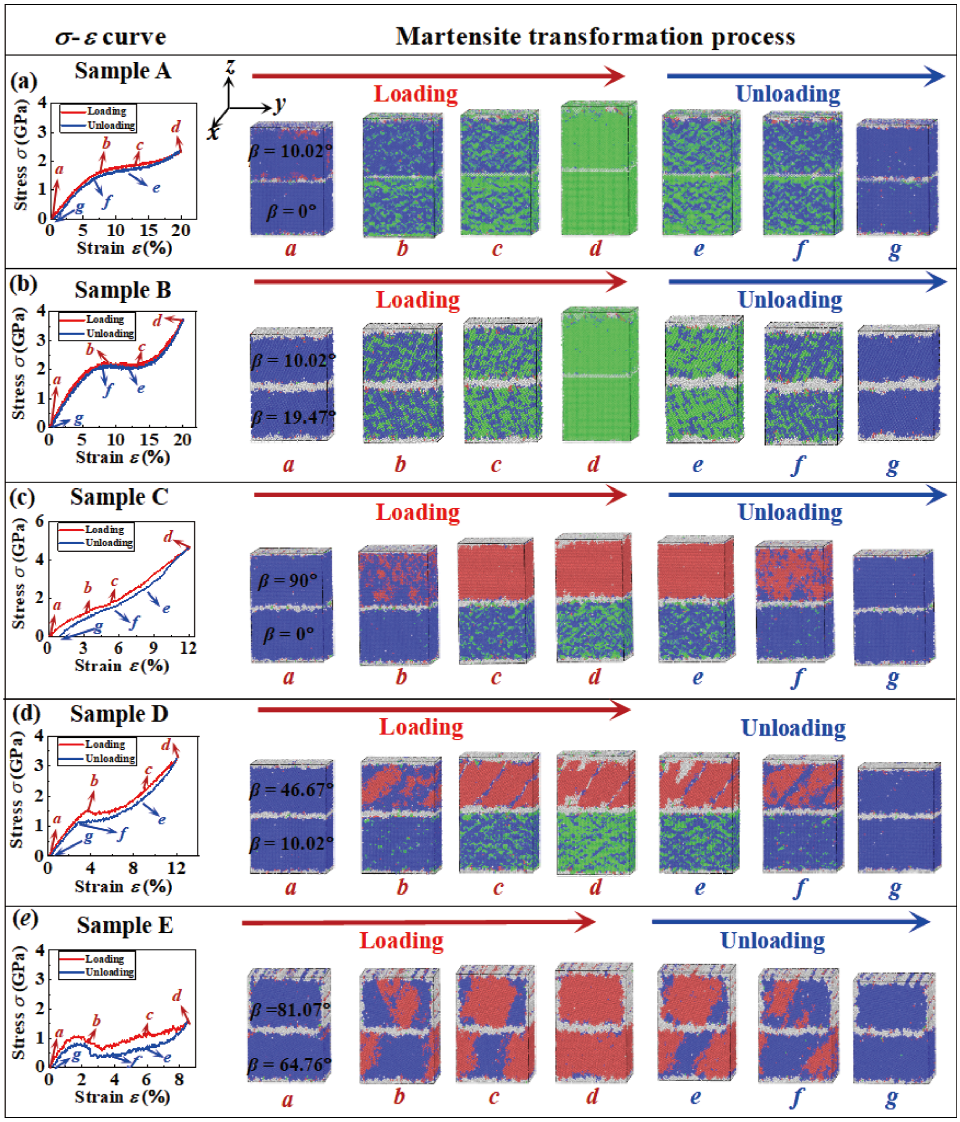

Figure 8 Stress-strain responses and atomic configurations of ATGB samples with different orientations under the tensile loading-unloading process along the *z*-axis. The blue, red, green and gray atoms correspond to the austenite (B2), martensite (B19'), martensite ($L1_0$), and disorder structures, respectively.

pathway B2 → B19' → B2 for the sample with $\beta \geq 35.26°$), the grains in both the STGB and ATGB samples with the same orientation category follow the same transformation pathway as the corresponding single crystal, such as STGB samples with $\beta \geq 35.26°$ as shown in Fig. 7(c)-(f). However, for the orientation categories II ($0° < \beta < 35.26°$), where the original single crystal takes the mixed transformation pathways B2 → $L1_0$ → B2 and B2 → B19' → B2, the grains in the bicrystal samples with the same orientation category adopt pathway B2 → $L1_0$ → B2. For example, both grains of the STGB sample with $\beta = 10.02°$ follow pathway B2 → $L1_0$ → B2 as shown in Fig. 7(a), instead of the mixed pathways B2 → $L1_0$ → B2 and B2 → B19' → B2 in the original single crystal. Based on the aforementioned phenomenon, it can be concluded that for the grains with the orientation categories I and II ($0° \leq \beta < 35.26°$), the grains of the bicrystal samples follow pathway B2 → $L1_0$ → B2. However, for the grains with the orientation category III ($35.26° \leq \beta \leq 90°$), the grains of the bicrystal samples take pathway B2 → B19' → B2.

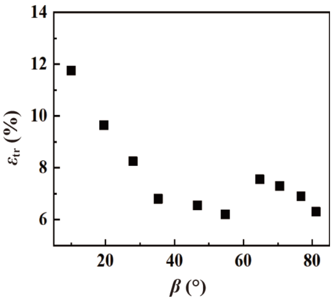

Figure 9 The dependence of transformation strain ε_{tr} of STGB samples with different orientations.

4. Discussions

4.1 Transformation strain prediction based on the maximum strain criterion

During the stress-induced phase transformation, the martensite variant that can induce the maximum strain among all possible variants would be the energetically favorable one to be transformed, since the formation of such martensite variant could be most effective in accommodating the applied stress field [12,58]. As a result, the preferred martensite variants can be determined based on this maximum strain criterion taking into account the lattice differences between the austenite and the possible martensite variants, then the corresponding transformation strains can be estimated. The transformation strain $\varepsilon_{\mathrm{tr}}$ in any tensile direction $\hat{\mathbf{n}}$ can be calculated as [12]

$$\varepsilon_{\mathrm{tr}} = \sqrt{\hat{\mathbf{n}} \cdot \left(\mathbf{U}_i^{\mathrm{T}} \mathbf{U}_i \hat{\mathbf{n}}\right)} - 1, \tag{1}$$

where $\mathbf{U}_i$ represents the transformation matrix that describes the deformation from the austenite to the martensite lattice, which can be derived from

$$\mathbf{e}_j^{mk} = \mathbf{U}_i \mathbf{e}_j^{a}, \tag{2}$$

where $\mathbf{e}_j^{a}$ and $\mathbf{e}_j^{mk}$ are the lattice vectors of the austenite and martensite phase, respectively (subscript j = 1, 2, 3, and superscript k = 1, 2 represent the B19’ and $\mathrm{L1_0}$ martensite, respectively). In this work, the B19’ monoclinic and $\mathrm{L1_0}$ tetragonal martensite phases have 12 and 3 variants, respectively. Therefore, the number of the matrix $\mathbf{U}_i$ between austenite and B19’ martensite phase is 12, and the number of the matrix $\mathbf{U}_i$ between austenite and $\mathrm{L1_0}$ martensite phase is 3 (where i = 1-12 and i = 13-15 for B19’ and $\mathrm{L1_0}$ martensite phase, respectively). The lattices of B2 austenite and V3 martensite variant are shown in Fig. 1(d) and (e), respectively. It can be seen that $\mathbf{e}_j^{a}$ and $\mathbf{e}_j^{m1}$ are

$$\begin{cases} \mathbf{e}_1^{a} = a_0(0,0,1), \\ \mathbf{e}_2^{a} = a_0(\bar{1},1,0), \\ \mathbf{e}_3^{a} = a_0(1,1,0), \end{cases} \text{and} \begin{cases} \mathbf{e}_1^{m1} = (0,0,a_{m1}), \\ \mathbf{e}_2^{m1} = \left(-\dfrac{\sqrt{2}}{2}b_{m1}, \dfrac{\sqrt{2}}{2}b_{m1}, 0\right), \\ \mathbf{e}_3^{m1} = \left[\dfrac{\sqrt{2}}{2}c_{m1} \times \cos\left(\theta - \dfrac{\pi}{2}\right), \dfrac{\sqrt{2}}{2}c_{m1} \times \cos\left(\theta - \dfrac{\pi}{2}\right), -c_{m1} \times \sin\left(\theta - \dfrac{\pi}{2}\right)\right]. \end{cases} \tag{3}$$

By introducing Eq. (3) into Eq. (2), one of matrix $\mathbf{U}_i$, i.e., matrix $\mathbf{U}_3$, is computed as an example, which describes the phase transformation between B2 austenite and a variant of B19’ martensite (V3).

$$\mathbf{U}_3 = \begin{pmatrix} \omega & \alpha & 0 \\ \alpha & \omega & 0 \\ -\gamma & -\gamma & \varphi \end{pmatrix}, \tag{4}$$

where $\omega = \dfrac{\sqrt{2}(b_{\mathrm{m1}} + c_{\mathrm{m1}}\sin\theta)}{4a_0}$, $\alpha = -\dfrac{\sqrt{2}(b_{\mathrm{m1}} - c_{\mathrm{m1}}\sin\theta)}{4a_0}$, $\gamma = \dfrac{c_{\mathrm{m1}}\cos\theta}{2a_0}$, $\varphi = \dfrac{a_{\mathrm{m1}}}{a_0}$. Here, the lattice parameters of austenite and the B19’ martensite phase are measured in this work as follows: a_0 = 0.3012 nm, a_{m1} = 0.2870 nm, b_{m1} = 0.4252 nm, c_{m1} = 0.4521 nm, θ = 96.8°. For the $\mathrm{L1_0}$ martensite phase, a_{m2} = 0.3401 nm, $b_{\mathrm{m2}} = c_{\mathrm{m2}}$ = 0.4056 nm, θ= 90°. The matrix $\mathbf{U}_i$ between austenite and B19’ and $\mathrm{L1_0}$ martensite phases is summarized in Tables 2 and 3, respectively.

Based on the maximum strain criterion and transformation pathway, the preferred martensite variants along each deformation direction can be determined as marked by black boxes in Fig. 5(b). In detail, for the sample with β = 0°, the $\mathrm{L1_0}$ tetragonal martensite variant $\mathrm{L1_0}$-1 can provide the maximum transformation strain (12.92%), which is larger than that of other variants, thereby the variant $\mathrm{L1_0}$-1 can be identified as the preferred martensite variant. This result is reasonable because the tensile loading ([001] direction) is along the long axis of the tetragonal variant $\mathrm{L1_0}$-1 as shown in Fig. 1(b). When 0° < β < 35.26°, there is an angle β between the loading direction (z-axis) and the austenite lattice direction ([001] direction) as shown in Fig. 1(c). The induced shear forces can drive the formation of B19’ martensite phase with a monoclinic lattice, despite its maximum transformation strain being smaller than that of the $\mathrm{L1_0}$ martensite phase with a tetragonal lattice. Therefore, in this case, combined with the presence of the shear forces and the maximum strain criterion, the preferred martensite variants are tetragonal variant $\mathrm{L1_0}$-1 and monoclinic variants V1 and V2 as shown marked by the black box in Fig. 5(b). For the samples with β ≥ 35.26°, the maximum transformation strain of B19’ martensite is larger than that of $\mathrm{L1_0}$ martensite, which indicates the B19’ martensite can completely replace the $\mathrm{L1_0}$ martensite phase as the preferred one. In this case, the B19’ martensite variants, which exhibit the highest transformation strain, are identified as the preferred martensite variants marked by the black box in Fig. 5(b). In detail, for the samples with (i) 35.26° ≤ β < 54.74°, variants V1 and V2 are the preferred martensite variants; (ii) β = 54.74°, the preferred variants are V1, V2, and V3; (iii)

Table 2 The lattice correspondence and transformation matrix $\mathbf{U}_i$ (i = 1-12) from austenite to B19' martensite variants

Variants	Lattice correspondence	$\mathbf{U}_i$

V1	$[010]_{B2}//[100]_{V1}$
	$[\bar{1}01]_{B2}//[010]_{V1}$
	$[101]_{B2}//[001]_{V1}$
		$\begin{pmatrix}\omega & 0 & \alpha\\ -\gamma & \varphi & -\gamma\\ \alpha & 0 & \omega\end{pmatrix}=\begin{pmatrix}1.0261 & 0 & 0.0278\\ 0.0888 & 0.9528 & 0.0888\\ 0.0278 & 0 & 1.0261\end{pmatrix}$

V2	$[100]_{B2}//[100]_{V2}$
	$[011]_{B2}//[010]_{V2}$
	$[0\bar{1}1]_{B2}//[001]_{V2}$
		$\begin{pmatrix}\varphi & -\gamma & -\gamma\\ 0 & \omega & \alpha\\ 0 & \alpha & \omega\end{pmatrix}=\begin{pmatrix}0.9528 & 0.0888 & 0.0888\\ 0 & 1.0261 & 0.0278\\ 0 & 0.0278 & 1.0261\end{pmatrix}$

V3	$[001]_{B2}//[100]_{V3}$
	$[\bar{1}10]_{B2}//[010]_{V3}$
	$[110]_{B2}//[001]_{V3}$
		$\begin{pmatrix}\omega & \alpha & 0\\ \alpha & \omega & 0\\ -\gamma & -\gamma & \varphi\end{pmatrix}=\begin{pmatrix}1.0261 & 0.0278 & 0\\ 0.0278 & 1.0261 & 0\\ 0.0888 & 0.0888 & 0.9528\end{pmatrix}$

V4	$[001]_{B2}//[100]_{V4}$
	$[\bar{1}10]_{B2}//[010]_{V4}$
	$[\bar{1}\bar{1}0]_{B2}//[001]_{V4}$
		$\begin{pmatrix}\omega & \alpha & 0\\ \alpha & \omega & 0\\ \gamma & \gamma & \varphi\end{pmatrix}=\begin{pmatrix}1.0261 & 0.0278 & 0\\ 0.0278 & 1.0261 & 0\\ -0.0888 & -0.0888 & 0.9528\end{pmatrix}$

V5	$[\bar{1}01]_{B2}//[100]_{V5}$
	$[010]_{B2}//[010]_{V5}$
	$[\bar{1}0\bar{1}]_{B2}//[001]_{V5}$
		$\begin{pmatrix}\omega & 0 & \alpha\\ \gamma & \varphi & \gamma\\ \alpha & 0 & \omega\end{pmatrix}=\begin{pmatrix}1.0261 & 0 & 0.0278\\ -0.0888 & 0.9528 & -0.0888\\ 0.0278 & 0 & 1.0261\end{pmatrix}$

V6	$[101]_{B2}//[100]_{V6}$
	$[010]_{B2}//[010]_{V6}$
	$[10\bar{1}]_{B2}//[001]_{V6}$
		$\begin{pmatrix}\omega & 0 & -\alpha\\ -\gamma & \varphi & \gamma\\ -\alpha & 0 & \omega\end{pmatrix}=\begin{pmatrix}1.0261 & 0 & -0.0278\\ 0.0888 & 0.9528 & -0.0888\\ -0.0278 & 0 & 1.0261\end{pmatrix}$

V7	$[101]_{B2}//[100]_{V7}$
	$[010]_{B2}//[010]_{V7}$
	$[\bar{1}01]_{B2}//[001]_{V7}$
		$\begin{pmatrix}\omega & 0 & -\alpha\\ \gamma & \varphi & -\gamma\\ -\alpha & 0 & \omega\end{pmatrix}=\begin{pmatrix}1.0261 & 0 & -0.0278\\ -0.0888 & 0.9528 & 0.0888\\ -0.0278 & 0 & 1.0261\end{pmatrix}$

V8	$[100]_{B2}//[100]_{V8}$
	$[01\bar{1}]_{B2}//[010]_{V8}$
	$[0\bar{1}\bar{1}]_{B2}//[001]_{V8}$
		$\begin{pmatrix}\varphi & \gamma & \gamma\\ 0 & \omega & \alpha\\ 0 & \alpha & \omega\end{pmatrix}=\begin{pmatrix}0.9528 & -0.0888 & -0.0888\\ 0 & 1.0261 & 0.0278\\ 0 & 0.0278 & 1.0261\end{pmatrix}$

V9	$[100]_{B2}//[100]_{V9}$
	$[011]_{B2}//[010]_{V9}$
	$[01\bar{1}]_{B2}//[001]_{V9}$
		$\begin{pmatrix}\varphi & -\gamma & \gamma\\ 0 & \omega & -\alpha\\ 0 & -\alpha & \omega\end{pmatrix}=\begin{pmatrix}0.9528 & 0.0888 & -0.0888\\ 0 & 1.0261 & -0.0278\\ 0 & -0.0278 & 1.0261\end{pmatrix}$

V10	$[100]_{B2}//[100]_{V10}$
	$[011]_{B2}//[010]_{V10}$
	$[0\bar{1}1]_{B2}//[001]_{V10}$
		$\begin{pmatrix}\varphi & \gamma & -\gamma\\ 0 & \omega & -\alpha\\ 0 & -\alpha & \omega\end{pmatrix}=\begin{pmatrix}0.9528 & -0.0888 & 0.0888\\ 0 & 1.0261 & -0.0278\\ 0 & -0.0278 & 1.0261\end{pmatrix}$

V11	$[001]_{B2}//[100]_{V11}$
	$[110]_{B2}//[010]_{V11}$
	$[1\bar{1}0]_{B2}//[001]_{V11}$
		$\begin{pmatrix}\omega & -\alpha & 0\\ -\alpha & \omega & 0\\ -\gamma & \gamma & \varphi\end{pmatrix}=\begin{pmatrix}1.0261 & -0.0278 & 0\\ -0.0278 & 1.0261 & 0\\ 0.0888 & -0.0888 & 0.9528\end{pmatrix}$

V12	$[001]_{B2}//[100]_{V12}$
	$[110]_{B2}//[010]_{V12}$
	$[\bar{1}10]_{B2}//[001]_{V12}$
		$\begin{pmatrix}\omega & -\alpha & 0\\ -\alpha & \omega & 0\\ \gamma & -\gamma & \varphi\end{pmatrix}=\begin{pmatrix}1.0261 & -0.0278 & 0\\ -0.0278 & 1.0261 & 0\\ -0.0888 & 0.0888 & 0.9528\end{pmatrix}$

Table 3 The lattice correspondence and transformation matrix $\mathbf{U}_i$ (i = 13-15) from austenite to $L1_0$ martensite variants

Variants	Lattice correspondence	$\mathbf{U}_i$

$L1_0$-1	$[100]_{B2}//[100]_{L1_0\text{-}1}$
	$[010]_{B2}//[010]_{L1_0\text{-}1}$
	$[001]_{B2}//[001]_{L1_0\text{-}1}$
		$\begin{pmatrix}\omega & 0 & 0\\ 0 & \omega & 0\\ 0 & 0 & \varphi\end{pmatrix}=\begin{pmatrix}0.9522 & 0 & 0\\ 0 & 0.9522 & 0\\ 0 & 0 & 1.1292\end{pmatrix}$

$L1_0$-2	$[010]_{B2}//[100]_{L1_0\text{-}2}$
	$[100]_{B2}//[010]_{L1_0\text{-}2}$
	$[001]_{B2}//[001]_{L1_0\text{-}2}$
		$\begin{pmatrix}\omega & 0 & 0\\ 0 & \varphi & 0\\ 0 & 0 & \omega\end{pmatrix}=\begin{pmatrix}0.9522 & 0 & 0\\ 0 & 1.1292 & 0\\ 0 & 0 & 0.9522\end{pmatrix}$

$L1_0$-3	$[001]_{B2}//[100]_{L1_0\text{-}3}$
	$[010]_{B2}//[010]_{L1_0\text{-}3}$
	$[100]_{B2}//[001]_{L1_0\text{-}3}$
		$\begin{pmatrix}\varphi & 0 & 0\\ 0 & \omega & 0\\ 0 & 0 & \omega\end{pmatrix}=\begin{pmatrix}1.1292 & 0 & 0\\ 0 & 0.9522 & 0\\ 0 & 0 & 0.9522\end{pmatrix}$

54.74° < β < 90°, the preferred variant is V3; and (iv) β = 90°, the preferred variants are V3 and V4. By comparing the theoretically predicted preferred variants in Fig. 5(b) with those observed in the MD simulation in Fig. 5(a), it is seen that the theoretical calculations are consistent with the MD simulation results.

Then, the transformation strain for each orientation can be predicted by combing the corresponding fraction of the preferred martensite variants f_i (see the values on the blocks in Fig. 5(a)) and the theoretical maximum transformation strain $\varepsilon_{\mathrm{tr}}^{i}$ (shown in the black box in Fig. 5(b)), as

$$\varepsilon_{\mathrm{tr}} = \sum f_i \times \varepsilon_{\mathrm{tr}}^{i}. \tag{5}$$

The transformation strain of samples can be calculated by Eq. (5) and plotted in Fig. 3(a), whose trend is consistent with the results of MD simulations. However, it is important to note that when $\beta \geq 35.26°$, the theoretical transformation strain $\varepsilon_{\mathrm{tr}}$ calculated using Eq. (5) slightly exceeds the MD results, with a maximum difference $\Delta\varepsilon_{\mathrm{tr}}$ of 1.35%. The possible explanation for this difference may be the persistence of untransformed austenite between different martensitic variants, as a typical example of β = 54.74° shown at "b" in Fig. 4(d). The volume fraction of each martensite variant f_i is computed as the ratio of the number of atoms in a single martensite variant N_i to the total number of martensite atoms N ($f_i = N_i / N$). Due to the omission of a small amount of residual austenite, N is slightly underestimated, leading to a slight overestimation of f_i. Consequently, this leads to a slight overestimation of the transformation strains in theoretical calculations.

4.2 The different transformation behaviors of bicrystal NiTi

The summary of the transformation pathways of bicrystal in Sect. 3.2 reveals that in bicrystal, the grains with orientation categories I and II follow pathway B2 → $L1_0$ → B2, whereas those within orientation category III take pathway B2 → B19' → B2. Therefore, for all STGB samples and ATGB samples with two grains sharing the same orientation category (i.e., ATGB samples A, B, E and F), two grains take the same transformation pathway, with the phase transformation occurring simultaneously in both grains, as shown in Figs. 7 and 8(a), (b) and (e). Meanwhile, the martensite variants in the bicrystal samples after transformation, as shown in Fig. 10, are consistent with those of single crystals with the same orientation as shown in Fig. 5 (a). Therefore, the transformation strain of this case is similar to that of the single crystal with the same orientation.

On the contrary, in the case of the ATGB sample that one grain with orientation categories I and II ($0° \leq \beta < 35.26°$) and another grain with orientation category III ($35.26° \leq \beta \leq 90°$), the two grains in ATGB sample take different transformation pathways. In this case, the phase transformation in one grain follows another one (does not happen simultaneously). In detail, the distribution of local shear strain and local shear stress of ATGB sample C and single crystal with $\beta = 64.76°$ are shown in Fig. 11. It shows that, in ATGB sample C, Grain 1 first takes transformation with pathway B2 → B19', while the elastic deformation of the austenite phase takes place in the Grain 2 at the same time as shown at $\varepsilon = 4.5\%$ (see Fig. 11). At the same time, the local strain increases not only in the phase transformation region in the Grain 1, but also in some regions of the austenite in the Grain 2 as marked by black circles. In contrast, the local strain and stress only increase in the phase transformation region of single crystal, as shown at $\varepsilon = 3.0\%$ and 4.8% in single crystal (see Fig. 11). Similarly, the local strain increases in the phase transformation region in Grain 2 and some regions of the B19' martensite phase, when the $L1_0$ martensite nucleates and grows in Grain 2 and the elastic deformation of B19' phase takes place in Grain 1 as shown at $\varepsilon = 10\%$. This complicate phenomenon induces that, the total transformation strain cannot be precisely measured from the macroscopic stress-strain curve, and it should be the result of the local transformation strain in each grain.

It is interesting that Grain 2 of the bicrystals prefers large elastic strain of austenite instead of triggering phase transformation, which seems resulted by its lower local stress than that in Grain 1, as the example shown by the local stress distribution with $\varepsilon = 4.5\%$ in Fig. 11. In addition, the

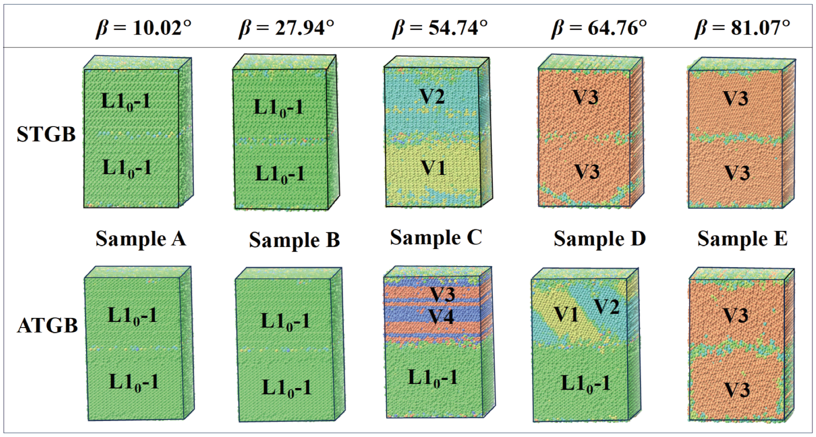

Figure 10 The variants distribution of the STGB and ATGB samples after loading.

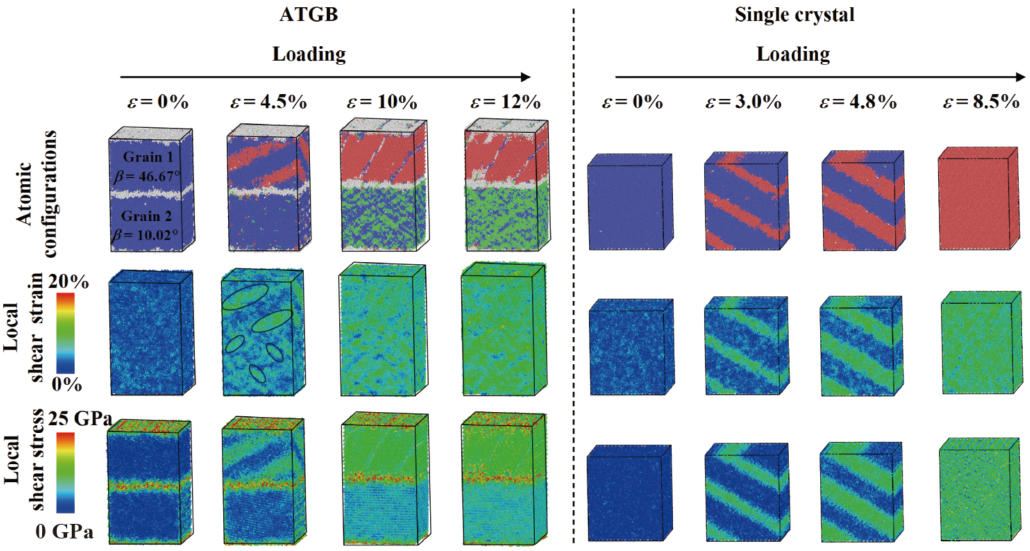

Figure 11 The atomic configurations, the local shear strain and the local shear stress of ATGB sample C and single crystal with $\beta = 64.76°$ under tensile loading. For the atomic configurations, the blue atoms, green atoms, and red atoms correspond to the B2 austenite phase, $L1_0$ tetragonal martensite phase, and B19' monoclinic martensite phase, respectively.

phase transformation in one grain results in stress softening [59,60], while the simultaneous elastic deformation in the other grain weakens this softening trend. Consequently, this interaction makes the macroscopic stress-strain responses prefer to a more linear one, as shown in Fig. 8(c)-(d). The in-depth physical mechanism deserves further study.

Similar to previous studies [25,43-45], the result in this work demonstrates that crystal orientation influences the transformation behavior, i.e., transformation pathways and the formation of martensitic variants, thereby affecting the mechanical properties of materials. Beyond studying several special crystal orientations, this work goes further by systematically analyzing the effect of crystal orientation on martensitic variants at an atomic scale. Additionally, it explores the correlation between the transformation pathway and transformation strain in single crystals and bicrystals SMA, obtaining high-performance bicrystals SMA based on the crystal orientation effect. Compared to the "S"-shaped stress-strain curves typically exhibited by conventional SMAs [61], the nearly linear stress-strain curves observed in the bicrystals SMA taking the dual-phase transformation, which might provide potential advantage accurate control in engineering applications. These interesting phenomena could be induced by the change of the transformation pathways between the individual single crystal and the corresponding grain due to the grain boundary effects.

5. Conclusion

In this work, the effect of transformation strain on crystal orientation of single crystal and bicrystal NiTi SMAs is systematically studied by molecular dynamics simulations. It is found that the crystal orientation-dependent transformation strain can be attributed to the transformation pathway and martensite variants in single crystal and bicrystal NiTi SMAs. The important conclusions can be drawn as follows:

(1) The orientation-dependent transformation strain of single crystal NiTi is influenced by the transformation pathways and martensite variants. The selection rule of the transformation pathway and preferred martensite variant that gives rise to the maximum transformation strains for each orientation is energetically preferred, which can be predicted theoretically based on the maximum strain criterion. Subsequently, the macroscopic transformation strain can be predicted by considering the theoretical transformation strain and the volume fraction of the preferred martensite variants, which is consistent with the results of MD in this work.

(2) The mechanical behavior of bicrystal NiTi depends on the synergistic effect of the transformation pathways in both single crystal grains. In all STGB samples and ATGB samples with two grains sharing the same orientation category, both grains take the same transformation pathway simultaneously, thereby leading to the transformation strain similar to those of the single crystal with the same orientation. For the case of the ATGB sample that one grain with orientation categories I and II and another grain with orientation category III, the ATGB sample takes different transformation pathways, and the synergistic effects of the transformation pathways in the two grains could result in a nearly linear stress-strain response.

Conflict of interest *On behalf of all authors, the corresponding author states that there is no conflict of interest.*

Author contributions ***Aimeng Zhang****: Conceptualization, Formal analysis, Writing – original draft.* ***Su Chen*** *and* ***Chenyang Du****: Formal analysis, Data curation.* ***Fa Wu*** *and* ***Shaobin Zhang****: Supervision, Conceptualization, Writing – review & editing.* ***Chun Li****: Investigation, Validation.*

Acknowledgements *This work was supported by National Natural Science Foundations of China (NSFC) (Grant Nos. 12372330, 11902257 and 12172293), Guangdong Basic and Applied Basic Research Foundation, China (Grant Nos. 2022A1515011308, 2022A1515010664 and 2022A1515010633), and the Fundamental Research Funds for the Central Universities.*

1 G. F. Ma, S. J. Qin, J. X. Shang, F. H. Wang, and Y. Chen, Atomistic study on the phase transformation in NiTi under thermal cycling, J. Alloys Compd. **705**, 218 (2017).
2 J. Mohd Jani, M. Leary, A. Subic, and M. A. Gibson, A review of shape memory alloy research, applications and opportunities, Mater. Des. (1980-2015) **56**, 1078 (2014).
3 S. Barbarino, E. I. Saavedra Flores, R. M. Ajaj, I. Dayyani, and M. I. Friswell, A review on shape memory alloys with applications to morphing aircraft, Smart Mater. Struct. **23**, 063001 (2014).
4 T. Ezaz, H. Sehitoglu, and H. J. Maier, Energetics of (114) twinning in B2 NiTi under coupled shear and shuffle, Acta Mater. **60**, 339 (2012).
5 M. Nishida, M. Matsuda, T. Fujimoto, K. Tanka, A. Kakisaka, and H. Nakashima, Crystallography of deformation twin boundaries in a B2 type Ti–Ni alloy, Mater. Sci. Eng. A **438-440**, 495 (2006).
6 G. Bihlmayer, R. Eibler, and A. Neckel, Martensitic phase transformation and electronic structure of NiTi and PdTi, Philos. Mag. B **73**, 511 (1996).
7 S. Kibey, H. Sehitoglu, and D. D. Johnson, Energy landscape for martensitic phase transformation in shape memory NiTi, Acta Mater. **57**, 1624 (2009).
8 K. Otsuka, and X. Ren, Physical metallurgy of Ti-Ni-based shape memory alloys, Prog. Mater. Sci. **50**, 511 (2005).
9 D. Schryvers, and P. L. Potapov, R-phase structure refinement using electron diffraction data, Mater. Trans. **43**, 774 (2002).
10 N. A. Zarkevich, and D. D. Johnson, Shape-memory transformations of NiTi: Minimum-energy pathways between austenite, martensites, and kinetically limited intermediate states, Phys. Rev. Lett. **113**, 1 (2014).
11 O. Matsumoto, S. Miyazaki, K. Otsuka, and H. Tamura, Crystallography of martensitic transformation in Ti Ni single crystals, Acta Metall. **35**, 2137 (1987).
12 K. Bhattacharya, in: Microstructure of Martensite: Why it Forms and How it Gives Rise to the Shape-Memory Effect (Oxford University Press, Oxford, 2003).
13 C. E. Sobrero, P. La Roca, A. Roatta, R. E. Bolmaro, and J. Malarría, Shape memory properties of highly textured Cu–Al–Ni–(Ti) alloys, Mater. Sci. Eng. A **536**, 207 (2012).

14 R. Lehnert, M. Müller, M. Vollmer, P. Krooß, G. Korpala, U. Prahl, M. Wendler, O. Volkova, T. Niendorf, H. Biermann, and A. Weidner, On the influence of crystallographic orientation on superelasticity-Fe-Mn-Al-Ni shape memory alloys studied by advanced in situ characterization techniques, Mater. Sci. Eng. A **871**, 144830 (2023).

15 J. Y. Chen, B. Q. Liu, L. L. Xing, W. Liu, L. P. Lei, and G. Fang, Toward tunable mechanical behavior and enhanced elastocaloric effect in NiTi alloy by gradient structure, Acta Mater. **226**, 117609 (2022).

16 A. Bauer, M. Vollmer, and T. Niendorf, Effect of crystallographic orientation and grain boundaries on martensitic transformation and superelastic response of oligocrystalline Fe–Mn–Al–Ni shape memory alloys, Shap. Mem. Superelast. **7**, 373 (2021).

17 L. W. Tseng, J. Ma, M. Vollmer, P. Krooß, T. Niendorf, and I. Karaman, Effect of grain size on the superelastic response of a FeMnAlNi polycrystalline shape memory alloy, Scr. Mater. **125**, 68 (2016).

18 F. H. Cao, Y. Chen, S. T. Zhao, E. Ma, and L. H. Dai, Grain boundary phase transformation in a CrCoNi complex concentrated alloy, Acta Mater. **209**, 116786 (2021).

19 Q. Zhu, A. Samanta, B. X. Li, R. E. Rudd, and T. Frolov, Predicting phase behavior of grain boundaries with evolutionary search and machine learning, Nat. Commun. **9**, 467 (2018).

20 Z. Wang, J. Chen, C. Besnard, L. Kunčická, R. Kocich, and A. M. Korsunsky, In *situ* neutron diffraction investigation of texture-dependent Shape Memory Effect in a near equiatomic NiTi alloy, Acta Mater. **202**, 135 (2021).

21 S. Dadbakhsh, B. Vrancken, J. P. Kruth, J. Luyten, and J. Van Humbeeck, Texture and anisotropy in selective laser melting of NiTi alloy, Mater. Sci. Eng. A **650**, 225 (2016).

22 N. Hatcher, O. Y. Kontsevoi, and A. J. Freeman, Role of elastic and shear stabilities in the martensitic transformation path of NiTi, Phys. Rev. B **80**, 1 (2009).

23 A. S. Mahmud, Z. G. Wu, H. Yang, and Y. N. Liu, Effect of cold work and partial annealing on thermomechanical behaviour of Ti-50.5at% Ni, Shap. Mem. Superelast. **3**, 57 (2017).

24 G. Q. Xie, F. Wang, X. Lai, Z. P. Xu, and X. G. Zeng, Atomistic study on crystal orientation-dependent crack propagation and resultant microstructure anisotropy in NiTi alloys, Int. J. Mech. Sci. **250**, 108320 (2023).

25 J. Y. Xiong, B. Xu, and G. Z. Kang, Phase field simulation on the martensite transformation and reorientation toughening behaviors of single crystal NiTi shape memory alloy: Effects of crystalline orientation and temperature, Eng. Fract. Mech. **270**, 108585 (2022).

26 X. Chen, X. Y. Wu, X. Yang, J. Wang, C. Lv, H. Zhang, X. Y. Pei, and F. Wang, Orientation-dependent multi-spall performance of monocrystalline NiTi alloys under shock compression, Mater. Today Commun. **40**, 109625 (2024).

27 X. Chen, Z. W. Wu, X. Tang, H. J. Hu, S. Lu, and H. P. Zheng, Orientation-dependent shock compression behavior of non-porous/porous NiTi shape memory alloy: An atomic scale study, Mater. Today Commun. **30**, 103114 (2022).

28 Y. C. Zhang, W. L. Yang, X. Yang, J. Wang, C. Lv, H. Zhang, X. Y. Pei, and F. Wang, Dynamic damage response of sing-crystal NiTi alloys induced by shear localization, Acta Mech. Sin. **41**, 124177 (2025).

29 Q. H. Kan, Y. Zhang, Y. G. Xu, G. Z. Kang, and C. Yu, Tension-compression asymmetric functional degeneration of super-elastic NiTi shape memory alloy: Experimental observation and multiscale constitutive model, Int. J. Solids Struct. **280**, 112384 (2023).

30 C. Yu, T. Zhou, Q. H. Kan, G. Z. Kang, and D. N. Fang, A two-scale thermo-mechanically coupled model for anomalous martensite transformation and elastocaloric switching effect of shape memory alloy, J. Mech. Phys. Solids **164**, 104893 (2022).

31 S. Dhala, S. Mishra, A. Tewari, and A. Alankar, Analyses of orientation dependent nanoindentation response of pseudoelastic NiTi alloy using a crystal plasticity model, Mech. Mater. **135**, 1 (2019).

32 Y. I. Chumlyakov, I. V. Kireeva, Z. V. Pobedennaya, L. P. Yakovleva, A. V. Vyrodova, and I. V. Kuksgauzen, Orientation dependence of shape memory effect and superelasticity in $(TiZrHf)_{50}Ni_{25}Co_{10}Cu_{15}$ high-entropy alloy single crystals, Shap. Mem. Superelast. **9**, 300 (2023).

33 L. W. Tseng, J. Ma, Y. I. Chumlyakov, and I. Karaman, Orientation dependence of superelasticity in FeMnAlNi single crystals under compression, Scr. Mater. **166**, 48 (2019).

34 J. Fornell, N. Tuncer, and C. A. Schuh, Orientation dependence in superelastic Cu-Al-Mn-Ni micropillars, J. Alloys Compd. **693**, 1205 (2017).

35 S. Liu, C. B. Ke, S. Cao, X. Ma, Y. F. Xu, and X. P. Zhang, A study of grain boundary effects on the stress-induced martensitic transformation and superelasticity in NiTi alloy via atomistic simulation, J. Appl. Phys. **133**, 085106 (2023).

36 X. F. Tao, Y. Yang, H. X. Zong, X. D. Ding, K. Y. Yu, T. Lookman, and J. Sun, Molecular dynamics simulations of ultralow hysteretic behavior in super-elastic shape memory alloys, Acta Mater. **232**, 117973 (2022).

37 M. Wang, S. Y. Jiang, Y. Q. Zhang, D. Sun, and B. Y. Yan, Molecular dynamics investigation on mechanical behaviour and phase transition of nanocrystalline NiTi shape memory alloy containing amorphous surface, Appl. Surf. Sci. **587**, 152871 (2022).

38 J. Y. Liu, Y. L. Deng, and X. B. Guo, Study the correlation of B19' phase transformation and grain orientation evolution on shape recovery of NiTi alloys fabricated by powder bed fusion, Mater. Charact. **205**, 113297 (2023).

39 B. F. Liu, Z. F. Li, W. Z. Li, Y. X. Pan, and W. P. Wu, Molecular dynamics simulation of the porosity effect on transformation mechanism of nanocrystalline porous NiTi shape memory alloy, Mater. Today Commun. **34**, 105320 (2023).

40 S. Liu, C. B. Ke, S. Cao, X. Ma, Z. X. Zhao, Y. W. Li, and X. P. Zhang, An atomistic study of self-accommodation martensite morphologies and microstructure evolution during forward and reverse martensitic transformations in single crystal and bicrystal NiTi alloys, Comput. Mater. Sci. **210**, 111455 (2022).

41 W. S. Choi, E. L. Pang, W. S. Ko, H. Jun, H. J. Bong, C. Kirchlechner, D. Raabe, and P. P. Choi, Orientation-dependent plastic deformation mechanisms and competition with stress-induced phase transformation in microscale NiTi, Acta Mater. **208**, 116731 (2021).

42 S. Alkan, A. Ojha, and H. Sehitoglu, The complexity of non-Schmid behavior in the CuZnAl shape memory alloy, J. Mech. Phys. Solids **114**, 238 (2018).

43 C. Yu, G. Z. Kang, Q. H. Kan, and D. Song, A micromechanical constitutive model based on crystal plasticity for thermo-mechanical cyclic deformation of NiTi shape memory alloys, Int. J. Plast. **44**, 161 (2013).

44 S. Y. Shuang, Y. X. Liang, C. Yu, Q. H. Kan, G. Z. Kang, and X. Zhang, Effect of loading orientation on plasticity in nano-laminated CoNiCrFeMn dual-phase high-entropy alloy: A molecular dynamics study, Model. Simul. Mater. Sci. Eng. **31**, 015005 (2023).

45 C. Yu, G. Z. Kang, and Q. H. Kan, A micromechanical constitutive model for anisotropic cyclic deformation of super-elastic NiTi shape memory alloy single crystals, J. Mech. Phys. Solids **82**, 97 (2015).

46 X. Zhang, S. J. Lu, B. Zhang, X. B. Tian, Q. H. Kan, and G. Z. Kang, Dislocation–grain boundary interaction-based discrete dislocation dynamics modeling and its application to bicrystals with different misorientations, Acta Mater. **202**, 88 (2021).

47 D. A. Wei, M. Zaiser, Z. Q. Feng, G. Z. Kang, H. D. Fan, and X. Zhang, Effects of twin boundary orientation on plasticity of bicrystalline copper micropillars: A discrete dislocation dynamics simulation study, Acta Mater. **176**, 289 (2019).

48 J. Y. Xiong, B. Xu, and G. Z. Kang, Phase field simulation on the grain orientation dependent super-elasticity of nanocrystalline NiTi shape memory alloy, Chin J. Solid Mech. **42**, 671-681 (2021).

49 W. S. Ko, B. Grabowski, and J. Neugebauer, Development and application of a Ni-Ti interatomic potential with high predictive accuracy of the martensitic phase transition, Phys. Rev. B **92**, 134107

(2015).
50 S. Plimpton, Fast parallel algorithms for short-range molecular dynamics, J. Comput. Phys. **117**, 1-19 (1995).
51 W. S. Ko, S. B. Maisel, B. Grabowski, J. B. Jeon, and J. Neugebauer, Atomic scale processes of phase transformations in nanocrystalline NiTi shape-memory alloys, Acta Mater. **123**, 90 (2017).
52 J. E. Dennis., D. M. Gay, and R. E. Walsh, An adaptive nonlinear least-squares algorithm, ACM Trans. Math. Softw. **7**, 348 (1981).
53 S. Ataollahi, and M. J. Mahtabi, Effects of precipitate on the phase transformation of single-crystal NiTi alloy under thermal and mechanical loads: A molecular dynamics study, Mater. Today Commun. **29**, 102859 (2021).
54 J. S. Lee, W. S. Ko, and B. Grabowski, Atomistic simulations of the deformation behavior of an Nb nanowire embedded in a NiTi shape memory alloy, Acta Mater. **228**, 117764 (2022).
55 W. S. Ko, W. S. Choi, G. L. Xu, P. P. Choi, Y. Ikeda, and B. Grabowski, Dissecting functional degradation in NiTi shape memory alloys containing amorphous regions via atomistic simulations, Acta Mater. **202**, 331 (2021).
56 B. Wang, G. Z. Kang, W. P. Wu, K. Zhou, Q. H. Kan, and C. Yu, Molecular dynamics simulations on nanocrystalline super-elastic NiTi shape memory alloy by addressing transformation ratchetting and its atomic mechanism, Int. J. Plast. **125**, 374 (2020).
57 B. F. Liu, Z. F. Li, C. Z. Du, and W. P. Wu, Molecular dynamics simulation of grain size effect on mechanism of twin martensite transformation of nanocrystalline NiTi shape memory alloys, Comput. Mater. Sci. **210**, 111451 (2022).
58 Y. Liu, The superelastic anisotropy in a NiTi shape memory alloy thin sheet, Acta Mater. **95**, 411 (2015).
59 D. J. Jiang, S. Kyriakides, C. M. Landis, and K. Kazinakis, Modeling of propagation of phase transformation fronts in NiTi under uniaxial tension, Eur. J. Mech.-A Solids **64**, 131 (2017).
60 J. F. Hallai, and S. Kyriakides, Underlying material response for Lüders-like instabilities, Int. J. Plast. **47**, 1 (2013).
61 S. W. Zhang, Z. D. Feng, S. Zhang, B. B. Zhang, W. Liu, N. B. Zhang, S. Chen, and S. N. Luo, Synchrotron-based multiscale study on phase transformation in a cold-rolled NiTi shape memory alloy: Effects of preexisting defects, Int. J. Mech. Sci. **238**, 107862 (2023).

基于晶体取向效应的NiTi形状记忆合金相变应变调控

张爱蒙, 陈苏, 杜晨阳, 吴法, 李春, 张少斌

摘要 等原子NiTi形状记忆合金(SMAs)可以从奥氏体发生多种马氏体相变路径, 这对其宏观性能, 特别是大变形/应变能力, 产生重要影响. 深入理解马氏体相和马氏体变体选择规则, 以及这些因素对SMA宏观力学行为的作用, 对于高性能SMA的设计与开发具有重要意义. 本研究结合分子动力学模拟与理论分析, 系统研究了单晶和双晶NiTi SMAs的相变路径、优选马氏体变体及其对宏观力学行为的影响. 结果表明, 晶体取向依赖的相变路径和马氏体变体显著影响单晶NiTi的相变应变. 此外, 在每种晶体取向下, 能量最优的相变路径和马氏体变体产生的相变应变最大, 这一规律能够通过理论分析进行预测, 并与分子动力学模拟结果高度一致. 此外, 双晶NiTi的应力-应变响应可以基于取向效应, 通过改变其相变路径进行调控. 本研究为晶体取向对NiTi的变形特性的影响提供了原子尺度的深入见解, 并为基于晶体取向调控高性能SMAs的设计提供了重要的理论依据.